Direct 2D spatial-coherence determination using the Fourier-analysis method: multi-parameter characterization of the P04 beamline at PETRA III

KAI BAGSCHIK,[1,*] JOCHEN WAGNER,[2] RALPH BUß,[2,3] MATTHIAS RIEPP,[1] ANDRÉ PHILIPPI-KOBS,[1] LEONARD MÜLLER,[1,4] JENS BUCK,[5] FLORIAN TRINTER,[1,6] FRANK SCHOLZ,[1] JÖRN SELTMANN,[1] MORITZ HOESCH,[1] JENS VIEFHAUS,[7] GERHARD GRÜBEL,[1,3] HANS PETER OEPEN,[2,3] AND ROBERT FRÖMTER[2,3]

[1]*Deutsches Elektronen-Synchrotron (DESY), Notkestraße 85, 22607 Hamburg, Germany*
[2]*INF, Universität Hamburg, CHyN, Luruper Chaussee 149, 22761 Hamburg, Germany*
[3]*The Hamburg Centre for Ultrafast Imaging, Luruper Chaussee 149, 22761 Hamburg, Germany*
[4]*Department of Physics, Universität Hamburg, Luruper Chaussee 149, 22761 Hamburg, Germany*
[5]*Institut für Experimentelle und Angewandte Physik, Leibnizstraße 19, 24098 Kiel, Germany*
[6]*Molecular Physics, Fritz-Haber-Institut der Max-Planck-Gesellschaft, Faradayweg 4, 14195 Berlin, Germany*
[7]*Helmholtz-Zentrum Berlin für Materialien und Energie GmbH, Albert-Einstein-Straße 15, 12489 Berlin, Germany*
[*]*Kai.Bagschik@desy.de*

Abstract: We present a systematic 2D spatial-coherence analysis of the soft-X-ray beamline P04 at PETRA III for various beamline configurations. The influence of two different beam-defining apertures on the spatial coherence properties of the beam is discussed and optimal conditions for coherence-based experiments are found. A significant degradation of the spatial coherence in the vertical direction has been measured and sources of this degradation are identified and discussed. The Fourier-analysis method, which gives fast and simple access to the 2D spatial coherence function of the X-ray beam, is used for the experiment. Here, we exploit the charge scattering of a disordered nanodot sample allowing the use of arbitrary X-ray photon energies with this method.

1. Introduction

To gain detailed knowledge of the coherence properties of X-ray radiation, its manipulation, and especially its preservation plays an increasingly important role at synchrotron beamlines, not least because of present and future upgrades of synchrotron facilities to diffraction-limited storage rings, e.g., PETRA IV [1], ALS-U [2,3], ESRF-EBS [4] or MAX IV [5]. The most obvious beneficiaries of a high coherent flux are coherent imaging and scattering experiments such as Fourier-transform holography (FTH) [6–9], X-ray ptychography [10–13], coherent diffractive imaging (CDI) [14–16], scanning transmission X-ray microscopy (STXM) [17–19], as well as X-ray photon correlation spectroscopy (XPCS) [20–22]. For these experiments, the knowledge of the intrinsic coherence properties of the X-ray source, as well as the impact of beamline apertures and optics, is essential for optimizing the experimental conditions and a correct interpretation of the data.

One important issue in this respect is whether the degree of coherence of the undulator beam can be transported without losses to these "coherent-flux-hungry" experiments. Beamline optics may cause a degradation of spatial coherence, e. g., due to imperfections of beryllium windows or of optics' surfaces, or vibrations of optical elements [23–28]. Another relevant question is how

Corrected: 14 May 2020

to determine the best beamline setting giving an optimized flux-coherence-balance of the beam for diverse experimental requirements. From these perspectives, detecting and understanding the coherence properties of the beam is of vital importance not only for planning experiments but also for the design and optimization of current and future beamlines.

Coherence-measurement techniques play a decisive role in this context as they are used to map out the effects of beamline optics and apertures on the coherence properties and ultimately to compare them with the theoretical expectations [29–31]. The requirements on these techniques have changed considerably over the last few years. Namely, they should be able to obtain reliably, fast, and with low effort, the full two-dimensional information about the spatial coherence properties of the beam. This is because a diagnostic measurement should not take away significant time from the actual experiments.

There exist a variety of techniques to determine the coherence properties of X-ray radiation, which can be divided into amplitude and intensity interferometry [32]. Amplitude interferometric techniques are based on amplitude-correlation measurements and thus on first-order correlation functions. The most prominent candidate is Young's double-pinhole experiment, but more advanced techniques have been developed over the last decades, which even allow for a direct two-dimensional analysis of the coherence properties in a short time, e.g., near-field speckle pattern analysis [33,34], circular phase-grating interferometry [35], or the Fourier-analysis method [36]. Intensity interferometry exploits second-order intensity correlation functions. This technique also allows for a two-dimensional analysis of the spatial coherence in a single measurement via analyzing intensity correlations at different relative positions across the beam [37,38].

In this paper, we present an in-detail multi-parameter 2D spatial-coherence analysis at the XUV variable-polarization beamline P04 at PETRA III [39]. The influence of two different beam-defining apertures, located at different positions along the beamline, on the photon-beam properties is studied in order to find optimal conditions for coherence-based experiments. In this study, the 2D spatial coherence, the photon-beam size at the focal position, and the photon flux are compared for various beam-defining aperture openings at three different photon energies. A significant reduction of the vertical spatial coherence compared to theoretical expectations is found and sources of this degradation are identified. We use the Fourier-analysis method detailed in [36] that allows for the determination of the full two-dimensional spatial (transverse) coherence function and hence the transverse coherence length of the X-ray radiation directly from a single far-field X-ray speckle pattern. Due to the simple and fast analysis, spatial-coherence measurements for various beamline settings can be carried out in a short time to optimize beam properties and re-check them during an experiment. The wavelength limitation present in our previous study [36] is overcome by using a nano-structured sample producing small-angle X-ray scattering from a charge inhomogeneity instead of a magnetic one. For this purpose, a highly spatially disordered nanodot array is used. Exploiting the small-angle X-ray scattering from a charge inhomogeneity for the Fourier-analysis method allows for a 2D spatial-coherence analysis not only for certain energies in the soft X-ray range, as in our previous study [36], but for arbitrary energies into the tender X-ray range, as presented here. Extension into hard X-rays should be feasible with adapted samples.

2. Experimental

2.1. Experimental setup and sample system

The experimental setup used for the spatial-coherence measurements is specifically designed for coherent small-angle X-ray scattering (SAXS) and X-ray holographic imaging (XHM) experiments at beamline P04 [36,40]. The sample is mounted on an aluminum sample holder and can be positioned using a piezoelectrically-driven positioning system. The SAXS pattern of the sample is detected by a Peltier-cooled 16 Mpx CCD camera with a pixel size of $15 \times 15 \, \mu m^2$ which

is positioned 90 cm downstream of the sample. The camera is protected from the high-intensity direct beam by a moveable central beam stop of 1 mm diameter. A 1 µm diameter pinhole can be inserted at the sample position to accurately scan the beam profile using a photodiode.

The sample could be any disordered system with a wide structural distance distribution like, e. g., colloidal gold nanoparticles, nanospheres, or lamellar structures. Here, we have used a spatially disordered nanodot array that is fabricated out of a homogeneous metallic multilayer $(Co_{1.65nm}/Pt_{2nm})_2$ via nanosphere lithography utilizing di-block copolymer micelles [41]. The multilayer is deposited on a 200 nm thick Si_3N_4 membrane of $500 \times 500 \, \mu m^2$ size.

The average size and distance distribution of the nanodots is determined by the core and/or shell diameter of the micelles [41,42]. Here, the nanodots have a diameter of ~ 20 nm. The distance distribution of the nanodots, obtained from a SEM image, is best described by the probability density function of the log-normal distribution, which is very similar to the gamma distribution (see Section 3.1). The distance distribution function has a maximum at a distance of 110 nm, a mean distance of 683 nm, and a standard deviation of 793 nm. The factor between standard deviation and mean distance is 1.16.

The distance distribution of the scattering objects, in this case the nanodots, plays an important role in the application of the Fourier-analysis method, as it determines the structure and shape of the autocorrelation function, i.e., the Patterson function, of the samples' electron density. In [36], we found that for gamma-distributed lamellar structures a factor between standard deviation and mean distance of larger than 0.5 is sufficient for the Fourier-analysis method. The Patterson function is in this case a constant except in the vicinity of the center. The center of the Patterson function shows an Airy-disk-like structure. The maximum radius of this structure is given by twice the size of the most prevalent spatial distance of the spatial-distance distribution, which is 110 nm in the here presented case. This radius has to be much smaller than the transverse coherence length of the beam so that the Airy disk-like structure does not affect the determination of the 2D spatial coherence function. Apart from that, the distance distribution determines the structure of the scattering pattern in reciprocal space. In case of the nanodot sample, a ring-shaped scattering pattern is obtained (see Section 3.1). Hence, the high-intensity region of the scattering signal is well-separated from the direct beam and the beam stop at the center of the scattering pattern. This separation is necessary, as sharp transitions and edges as well as parasitic scattering around the beam-stop may cause unwanted artefacts in the Fourier transform of the scattering pattern. As a consequence, a uniform distance distribution of scatterers would be unsuitable for the Fourier-analysis method.

2.2. Beamline layout

The experiments have been performed at the XUV variable polarization beamline P04 at PETRA III, delivering photon energies ranging from 250 eV to 3000 eV [39]. High-brilliance soft X-ray radiation is generated via a 4.9 m long APPLE-II type helical undulator. The beamline layout is shown in Fig. 1. A beam-defining four-blade aperture (BDA) located 27.9 m downstream of the undulator source is used to define the angular acceptance of the beamline and to select a coherent volume of the beam used for the experiment. The photon beam can be switched between two branches using a switching mirror unit (SMU) located 35 m downstream of the undulator. In Fig. 1 only the branch used for the presented experiments is shown. The undulator beam is monochromatized using a plane mirror/varied- line-spacing (VLS) plane grating (PM/PG-U) unit 46 m downstream of the undulator. The VLS grating disperses the beam vertically and focusses it in the vertical direction into the plane of an exit-slit unit (EXSU). The vertical exit aperture monochromatizes the beam by spatially filtering the spectral focal curve and thus defines the resolving power. As a consequence, the longitudinal coherence of the beam is improved. A vertical exit-slit of 30 µm width, yielding a resolving power of around $\lambda/\Delta\lambda = 10^4$ has been used for the experiments, resulting in a longitudinal coherence length in the order of $l_c = 10$–20 µm.

This is a factor 50 larger than the maximum path-length difference in the experiment and had thus no sizeable impact on the experimental results. The horizontal blades at the EXSU can be used to select the coherent volume of the photon beam in horizontal direction at a larger distance from the undulator source compared to the BDA. The beam is focused in vertical and horizontal direction to the experimental platform using a Kirkpatrick-Baez (KB) mirror system consisting of two plane-elliptical mirrors located 78.5 m (VKB) and 79.1 m (HKB) downstream of the undulator, respectively. In the horizontal direction, the undulator source is directly imaged to the experiment focus with a demagnification factor of around 40. In the vertical direction, the exit slit of the monochromator is imaged to the experiment focus with a demagnification factor of 3. This results in a minimum focal spot size of $10\,\mu m \times 10\,\mu m$ for a $30\,\mu m$ vertical exit-slit opening.
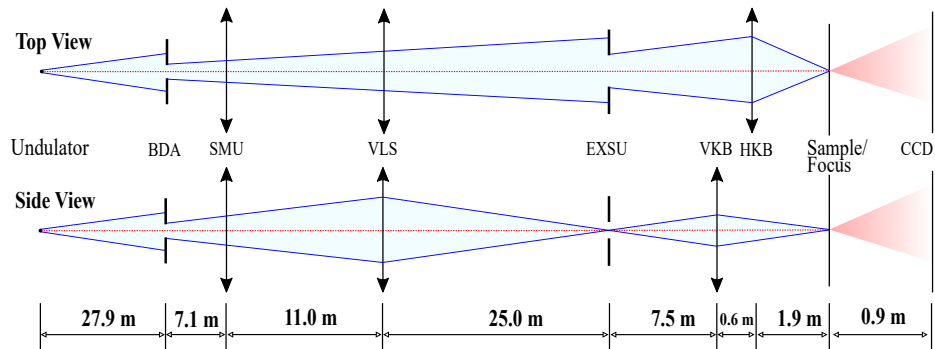
Fig. 1. Arrangement of the optical elements of the P04 beamline at PETRA III. The beamline consists of an APPLE-II type undulator, beam-defining apertures (BDA), a switching mirror unit (SMU), a varied-line-spacing (VLS) grating, an exit-slit aperture (EXSU), a vertical (VKB), and horizontal (HKB) refocusing mirror. The small-angle scattering pattern of the sample positioned in the focus is recorded with a CCD detector.

3. Theory

3.1. *Small-angle X-ray scattering with partially spatially coherent X-ray beams*

SAXS is typically used to investigate objects containing structural features on a 100 nm length scale [43]. It is a highly versatile ensemble-averaging technique for the structural characterization of nanomaterials probing structural features over a sample volume typically much larger than the characteristic structure sizes under investigation. The spatial coherence properties of the illuminating beam have direct impact on the far-field SAXS pattern. Coherent illumination results in the emergence of speckles. For extended samples, the angular width of the speckles is determined by the size of the illuminating beam and its spatial coherence properties. The scattering pattern of an object with electron density $\rho(\mathbf{r})$ under partially spatial coherent illumination is described by [44,45]

$$I(\mathbf{q}) = \iint J(\mathbf{r}_1, \mathbf{r}_2)\, \rho(\mathbf{r}_1)\, \rho(\mathbf{r}_2)\, e^{-i\mathbf{q}(\mathbf{r}_1 - \mathbf{r}_2)} d\mathbf{r}_1 d\mathbf{r}_2, \tag{1}$$

where $\mathbf{r} = (x, y)$ is a two-dimensional vector in the sample plane. The function $J(\mathbf{r}_1, \mathbf{r}_2)$ is called mutual optical intensity (MOI) and is an equal-time correlation function describing the spatial coherence of the illuminating field in the quasi-monochromatic approximation. The quasi-monochromatic approximation can be applied in case of a narrow spectral bandwidth $\Delta E \ll E$ of the X-ray radiation. In this case, the longitudinal coherence length l_c is much larger than any path-length difference occurring in the experiment, which makes temporal- coherence

effects negligible. Within the framework of the Gaussian Schell-model (GSM) [46], the MOI can be expressed by

$$J(\mathbf{r}_1, \mathbf{r}_2) = \sqrt{I(\mathbf{r}_1)}\sqrt{I(\mathbf{r}_2)}\mu(\mathbf{r}_1 - \mathbf{r}_2), \tag{2}$$

where $\mu(\mathbf{r}_1 - \mathbf{r}_2)$ is the complex degree of coherence, or complex coherence factor (CCF). $I(\mathbf{r}_1)$ and $I(\mathbf{r}_2)$ are the intensity values of the incoming beam at points $\mathbf{r}_1$ and $\mathbf{r}_2$. The GSM is a successful approach to describe the spatial coherence of synchrotron radiation, as both the intensity and the CCF are well described by Gaussian functions. Substitution of Eq. (2) into Eq. (1) and using $\Delta\mathbf{r} = \mathbf{r}_1 - \mathbf{r}_2$ yields [36]

$$
\begin{aligned}
I(\mathbf{q}) &= \int \left\{ \int \sqrt{I(\mathbf{r}_1)}\rho(\mathbf{r}_1) \sqrt{I(\mathbf{r}_1 - \Delta\mathbf{r})}\rho(\mathbf{r}_1 - \Delta\mathbf{r})\,d\mathbf{r}_1 \right\} \mu(\Delta\mathbf{r})e^{-i\mathbf{q}(\Delta\mathbf{r})}d\Delta\mathbf{r} \\
&= \int O(\Delta\mathbf{r})\mu(\Delta\mathbf{r})e^{-iq(\Delta r)}d\Delta\mathbf{r}
\end{aligned}
. \tag{3}
$$

The function $O(\Delta\mathbf{r})$ is the autocorrelation of the product of the electron density and the intensity distribution of the illuminating beam. Using the convolution theorem [44], the scattering intensity in Eq. (3) can be described by

$$I(\mathbf{q}) = I_{\text{coh}}(\mathbf{q}) \otimes \mu(\mathbf{q}), \tag{4}$$

where $\mathbf{q}$ is a two-dimensional scattering vector with $|\mathbf{q}| = 4\pi\sin(\theta)/\lambda$, λ is the wavelength and $2\cdot\theta$ is the scattering angle. $I_{\text{coh}}(\mathbf{q}) = \mathcal{F}\{O(\Delta\mathbf{r})\}$ is the diffraction pattern produced by a fully coherent incident Gaussian beam and $\mu(\mathbf{q})$ the Fourier transform of the CCF. Within the GSM, the CCF $\mu(\Delta\mathbf{r})$ is a Gaussian function with an rms width l_s, which is the transverse coherence length. Consequently, $\mu(\mathbf{q})$ is also a Gaussian function in reciprocal space with an rms width $w_s = 2\pi/l_s$. Within the framework of the GSM, a global degree of coherence or coherent fraction can be introduced, which characterizes the spatial coherence properties of the photon beam by one scalar number [36,47]

$$\zeta = \frac{h}{\sqrt{4 + h^2}}, \tag{5}$$

where $h = l_s/\sigma_b$ and σ_b is the rms width of the photon beam. ζ varies from zero for incoherent to one for fully coherent radiation. It can be factorized and calculated separately for the horizontal ζ_x and vertical ζ_y directions. The total degree of coherence or total coherent fraction is given by the product $\zeta = \zeta_x\zeta_y$ of both components.

The modeling of a SAXS experiment including beam size and spatial coherence is presented in Fig. 2. For this, a scanning electron microscopy (SEM) image of the nanodot sample [see Fig. 2(a)] is binarized and multiplied with the square root of the photon beam profile, assumed to be Gaussian. Figure 2(b) shows the spatial-distance distribution of the nanodot sample, which is reasonable well described by the probability density function of the log-normal distribution. The FWHM of the modeled beam is 10 µm × 10 µm (4.25 µm × 4.25 µm, rms) in horizontal and vertical directions. Subsequently, the modulus square of the Fourier transform of the product of both functions results in $I_{\text{coh}}(\mathbf{q})$ [see Fig. 2(e)]. In order to take the spatial coherence properties of the photon beam into account $I_{\text{coh}}(\mathbf{q})$ is convolved with the Fourier transform of the CCF, $\mu(\mathbf{q})$, [see Fig. 2(c)] according to Eq. (4). Figure 2(e) shows modeled SAXS patterns for four different cases of global degree of coherence in horizontal in vertical directions. In case of full spatial coherence, the SAXS pattern shows a sharp and grainy speckle pattern. In case of low spatial coherence, either in horizontal or vertical direction, the speckles are elongated and streaky in horizontal or vertical direction, respectively. The lower right quadrant in Fig. 2(e) shows the pattern for an intermediate case of spatial coherence, where the speckles are larger in size in both directions compared to the fully coherent case.
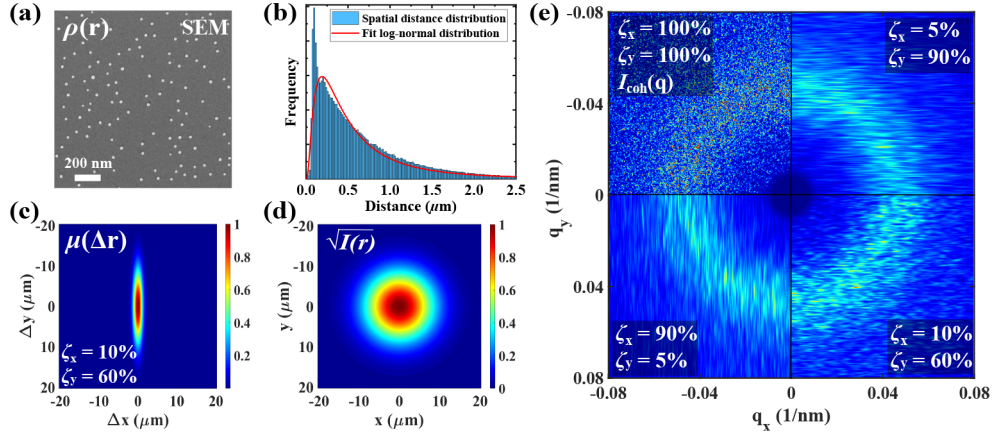
Fig. 2. (a) Small section of a scanning electron microscopy (SEM) image of the spatially disordered nanodot array. (b) Spatial-distance distribution of the nanodot array (blue bars), reasonably well described by the probability density function of a log-normal distribution (red curve). (c) Modeled two-dimensional complex coherence factor (CCF) of the $10 \times 10\,\mu m^2$ photon beam having a horizontal spatial coherence of 10% and a vertical spatial coherence of 60%. (d) Square-root of the two-dimensional photon beam intensity assuming a Gaussian profile. (e) Modeled small-angle scattering (SAXS) pattern for four different spatial coherence conditions using a binarized version of the full SEM image ($40\,\mu m^2$), the two-dimensional beam profile and the complex coherence function of the photon beam given in Eq. (3).

3.2. Fourier-analysis method

Here, the Fourier-analysis method described in [36] is applied to the charge scattering from a disordered ensemble of metallic nanodots. In contrast to using magnetic domain patterns of laterally homogeneous films where the resonant interaction via the X-ray magnetic circular dichroism (XMCD) effect is utilized as scattering contrast, this gives access to the two-dimensional spatial coherence properties of X-ray radiation without restrictions to specific photon energies. The scattered intensity distribution of the spatially disordered sample under partially spatially coherent illumination, as measured by the detector, is described by Eq. (3). The inverse Fourier transform of Eq. (3) yields

$$I_F(\Delta \mathbf{r}) = \left| \mathcal{F}^{-1} \left\{ \int O(\Delta \mathbf{r}) \mu(\Delta \mathbf{r}) e^{-iq(\Delta \mathbf{r})} d\Delta \mathbf{r} \right\} \right| = |O(\Delta \mathbf{r})||\mu(\Delta \mathbf{r})|. \tag{6}$$

Equation (6) implies that the inverse Fourier transform of the nanodot scattering pattern $I_F(\Delta \mathbf{r})$ is the product of the modulus of the CCF, $\mu(\Delta \mathbf{r})$, and the modulus of the product autocorrelation function of the electron density $\rho(\mathbf{r})$ of the scattering object, i.e., the Patterson function, and the intensity distribution of the illuminating beam $I(\mathbf{r})$, $O(\Delta \mathbf{r})$. It has been verified by simulations [36] that the product autocorrelation function $O(\Delta \mathbf{r})$ can be separated into the product of the Patterson function of the electron density $P(\Delta \mathbf{r})$ and the autocorrelation function of the beam intensity distribution $\Psi(\Delta \mathbf{r})$. The latter is feasible in the here-presented case, where the electron density is a spatially fast varying function and the intensity distribution a spatially slow varying function. The former prerequisite is also fulfilled by the magnetic scattering density of a disordered magnetic maze-domain pattern as shown in [36]. Hence, Eq. (6) can be expressed as

$$I_F(\Delta \mathbf{r}) = |P(\Delta \mathbf{r})||\Psi(\Delta \mathbf{r})||\mu(\Delta \mathbf{r})| \tag{7}$$

The Patterson function of the spatially disordered nanodot array is constant, except for a tiny region in the vicinity of the center, and thus contributes to $I_F(\Delta \mathbf{r})$ only by a constant multiplicative

factor. Consequently, Eq. (7) can be used to deduce the two-dimensional representation of $\mu(\Delta\mathbf{r})$ in a particularly simple way, which in turn can be utilized to determine the transverse coherence length l_s of the illuminating beam.

The results of the Fourier-analysis method applied to the above-modeled SAXS pattern (Fig. 2) are shown in Fig. 3. Figure 3(a) depicts the case of full spatial coherence ($\zeta_{x,y} = 100\%$) and Fig. 3(b) the case of intermediate spatial coherence. In Fig. 3(a), $I_F(\Delta\mathbf{r})$ represents $\Psi(\Delta\mathbf{r})$ except for a constant multiplicative factor. For the intermediate case, an rms width of $l_{s,x} = 0.85$ μm in horizontal and $l_{s,y} = 6.36$ μm in vertical direction is used as input parameters for $\mu(\Delta\mathbf{r})$ according to a global degree of coherence of $\zeta_x = 10\%$ in horizontal and $\zeta_y = 60\%$ in vertical direction [see Fig. 2(c) and Section 3.1]. It can be clearly seen that in the case of a low spatial coherence along the horizontal direction, the Gaussian $\mu(\Delta x)$ strongly dominates the Fourier-transformed speckle pattern $I_F(\Delta x)$. In Fig. 3(c), the CCF of the pattern shown in Fig. 3(b) in horizontal $\mu(\Delta x)$ (red curve) and vertical direction $\mu(\Delta y)$ (blue curve) is presented. These functions are obtained from the normalization of $I_F(\Delta x)$ and $I_F(\Delta y)$ using $\Psi(\Delta x)$ and $\Psi(\Delta y)$ [36]. A Gaussian fit to the profiles results in $l_{s,x} = (0.91 \pm 0.01)$ μm and $l_{s,y} = (6.17 \pm 0.04)$ μm in horizontal and vertical directions, respectively. The obtained results are in very good agreement with the input parameters used for the convolution of the SAXS pattern above (see Section 3.1). Hence, this shows that the method is able to extract the entire information about the two-dimensional spatial coherence of the illuminating beam from a single SAXS pattern.
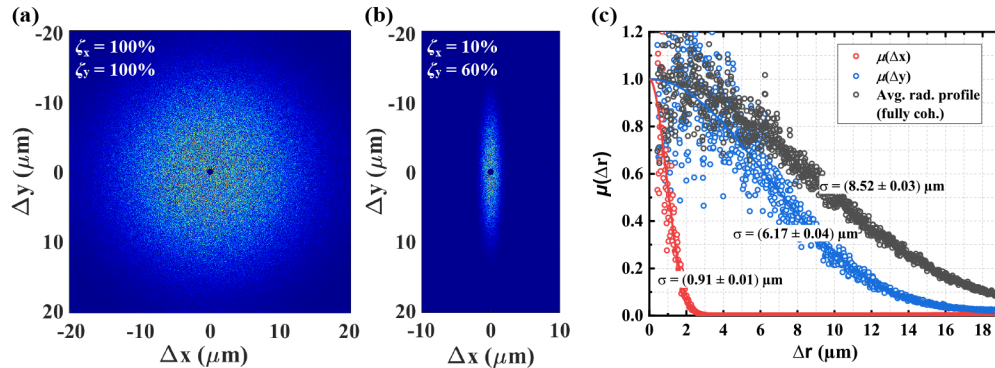
Fig. 3. (a) Inverse Fourier transform of the modeled SAXS patterns assuming (a) a fully spatially coherent photon beam and (b) a horizontal spatial coherence of 10% and a vertical spatial coherence of 60%. (c) The CCF given by central line profiles across the pattern shown in (b) in horizontal (red open circles) and vertical (blue open circles) directions. The gray curve is obtained by azimuthally averaging the pattern in (a). The rms values σ are obtained from a Gaussian fit to the data (colored lines). One can see that the horizontal profile is highly dominated by the CCF in the horizontal direction.

4. Results

### 4.1. Spatial-coherence measurements at the beamline P04 at PETRA III

The two-dimensional spatial-coherence properties of the photon beam at the P04 beamline at PETRA III is determined using the Fourier-analysis method. For this, single-exposure SAXS patterns from the spatially disordered nanodot sample [see Fig. 2(a)] are recorded with the CCD detector. The exposure time is varied between 5 ms and 6 s, depending on beamline settings. The beam profile is obtained via scanning the beam in the focus with a 1-μm- diameter pinhole. Figure 4 shows two SAXS patterns, $I(\mathbf{q})$, recorded at a photon energy of 500 eV and their corresponding Fourier-transformed patterns $I_F(\Delta\mathbf{r})$. The slightly anisotropic shape

of the SAXS patterns compared to the modeled pattern in Fig. 2(e) originates from a slightly anisotropic distance distribution of the nanodots at the illuminated sample location. This has no notable impact on the Patterson function particularly at large $\Delta\mathbf{r}$, where it is constant. The two patterns displayed in the left and right half of the images show two different cases of spatial coherence. The right half corresponds to illumination with the full beam. Elongated speckles along the horizontal direction are observed indicating a low spatial coherence in that direction. The left half shows a scattering pattern from the same sample when the photon beam is cut by the horizontal BDA [see Fig. 1], set to 200 µm. The FWHM of the photon beam at the BDA position is around 800 µm (central radiation cone). Thus, the cutting results in a drop in photon flux by one order of magnitude. Round speckles (decreased speckle size along the horizontal direction) can be seen in the left half of Fig. 4(a), reflecting the increased spatial coherence in that direction. This is in agreement with the predictions of the model data presented in Section 3.2. An inverse Fourier transform of the SAXS patterns yields the above-described product of the spatial coherence, Patterson, and autocorrelation function of the beam profile [see Fig. 4(b)]. It can be clearly seen that the profile in the right part of Fig. 4(b) is strongly asymmetric and dominated by the limited spatial coherence in the horizontal direction as described in Appendix A. In contrast, the left half of Fig. 4(b) is almost isotropic due to the increased spatial coherence in the horizontal direction. The high-intensity horizontal streak in the center of both patterns originates from the beam-stop wire half-traversing the SAXS pattern in the vertical direction [see Fig. 4(a)]. The radial CCF profiles for both two-dimensional patterns shown in Fig. 4(b) as a function of angular direction are obtained from azimuthally averaged circle segments of 10° width using the procedure given in [36]. The horizontal CCF profiles in case of the full beam and for the horizontal 200 µm BDA are presented in Fig. 5(a). A Gaussian fit to the CCFs is used to determine the transverse coherence length (rms width of the Gaussian function). The horizontal transverse coherence length of the full beam is $l_{s,x} = (1.18 \pm 0.04)$ µm, and with the BDA set to 200 µm in the horizontal direction $l_{s,x} = (4.37 \pm 0.05)$ µm. Hence, the transverse coherence length could be increased by a factor of 3.7. The data shows an increase of the CCF at larger separations Δx, after the initial falloff, which is frequently reported in literature [47–50]. The CCF increases above $\Delta x = 3$ µm in case of the full beam and above $\Delta x = 8.5$ µm for the horizontal 200 µm BDA [Fig. 5(a)]. In accordance with literature, only the central lobe has been fitted with a Gaussian in order to determine the transverse coherence length [12,47,50]. It has been suggested that the increase of the CCF at larger $\Delta\mathbf{r}$ arises from the contribution of higher residual coherence modes to the fundamental coherent mode [51]. Figure 5(b) displays the transverse coherence length in all angular directions. The regions shaded in grey mark the angle where the two-dimensional profile is corrupted due to the impact of the beam-stop wire. An elliptical fit to the data excluding corrupted data points is used to calculate the values of the global degree of coherence in horizontal and vertical directions. For the case of the full beam, the horizontal and vertical global degrees of coherence are $\zeta_x = (13 \pm 1)\%$ and $\zeta_y = (50 \pm 3)\%$, respectively. For the horizontal 200 µm BDA, the horizontal and vertical global degree of coherence are $\zeta_x = (46 \pm 3)\%$ and $\zeta_y = (53 \pm 3)\%$, respectively, which is almost isotropic. The observed correlation between the SAXS pattern (shape of speckles) and the obtained values of the global degree of coherence are in a good agreement with the predictions of the model data presented in Sections 3.1 and 3.2.

4.2. *Two-dimensional multi-parameter spatial-coherence analysis*

In the following, a systematic spatial-coherence analysis of P04 is performed in order to find optimal beamline configurations for coherence-based experiments and to identify different origins of decoherence effects. The presented analysis can be used as a guideline for other beamlines on how to determine, understand, and possibly improve the spatial-coherence properties. Prior to such an experimental study, it is useful to calculate the coherence properties of the available undulator source (see Appendix A). This provides an initial estimate of the expected global
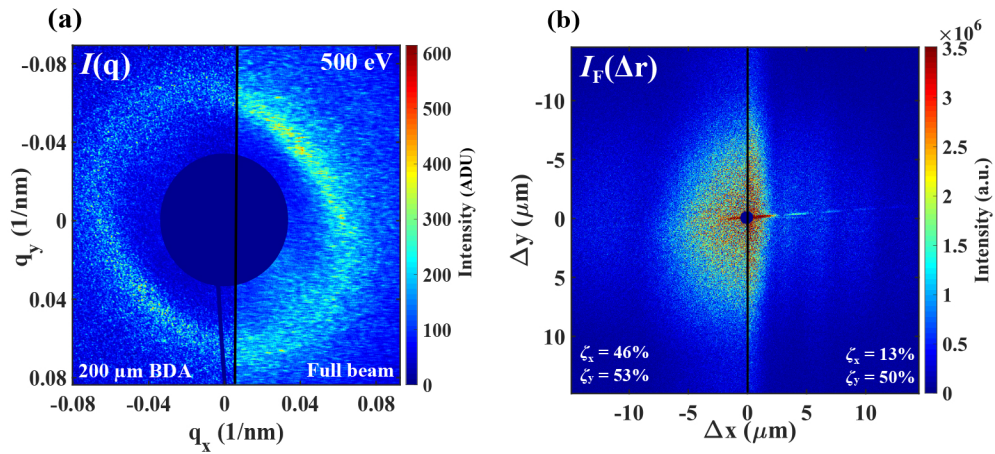
Fig. 4. (a) SAXS pattern recorded at the P04 beamline at a photon energy of 500 eV from the spatially disordered nanodot sample. In the left half image, the horizontal BDA aperture has been closed to 200 μm, while in the right half image the full beam is impinging on the sample. (b) Fourier transform of the SAXS pattern shown in (a) that has been used to determine the transverse coherence in all angular directions. The values of the global degree of coherence for the horizontal and vertical directions are given in the figure.
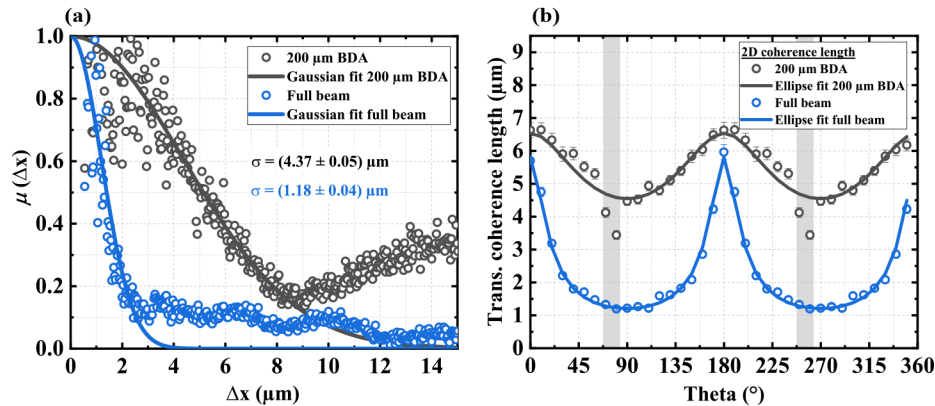
Fig. 5. (a) Complex coherence factors (CCFs) along the horizontal direction extracted from the two-dimensional spatial coherence functions determined at a photon energy of 500 eV [see Fig. 4(b)]. The profiles show an increase of the CCF at $\Delta x = 3$ μm for the full beam and at $\Delta x = 8.5$ μm for the 200 μm BDA. For the analysis, a Gaussian fit to the central lobe of the data has been performed in order to determine the transverse coherence length. (b) Transverse coherence length determined in all angular directions. An ellipse has been fitted to the data in order to determine the global degree of coherence in horizontal and vertical directions [see Fig. 4]. The angular regions shaded in gray have been omitted in the fit, as here the two-dimensional profile is corrupted due to the impact of the beam-stop wire on the Fourier-transformed SAXS pattern [see Figs. 4(a) and 4(b)].

degree of coherence of the synchrotron radiation. At P04 the coherent fraction from the source is about 90% in the vertical direction and between 4% and 20% in the horizontal direction for the photon energy range covered by the beamline (see Appendix A). In order to increase the total coherent fraction available for an experiment, a straightforward approach is to use a slit system in the horizontal direction, downstream from the undulator, to cut out a coherent portion of the beam.

For the systematic spatial-coherence analysis of P04, three different photon energies (500 eV, 780 eV, and 1200 eV) and different beamline configurations are used and compared in terms of photon flux, spatial coherence, and focal beam size. Two horizontal beam-defining apertures (BDA, EXSU) at two different positions (27.9 m and 71 m) downstream from the undulator [see Fig. 1] are used as spatial coherence filter and/or secondary source.

The horizontal beam-defining apertures BDA and EXSU at beamline P04 generally have a different impact on the beamline parameter under investigation. The BDA close to the undulator source can be used as a spatial coherence filter and as a secondary source. Thus, it controls the beam´s spatial-coherence properties as well as the focal spot size at the experiment. The EXSU beam-defining aperture close to the refocusing mirror unit can be used also as a spatial coherence filter, while the focal spot size remains determined by the geometrical demagnification of the undulator or secondary source, the latter defined by the BDA. The difference between those two apertures can be explained by Fresnel and Fraunhofer diffraction from the apertures analyzed at the focal position and characterized by the Fresnel number N_F [52] ($N_F > 1$ Fresnel, $N_F \ll 1$ Fraunhofer). Due to the small distance of the EXSU aperture to the focal position (10 m) the Fresnel number ranges from $N_F = 570$ to $N_F = 1.5$ at 780 eV photon energy for the aperture sizes between 6 mm and 300 µm used for the spatial coherence analysis. In this range of N_F (Fresnel diffraction) the shape and divergence of the beam downstream of the aperture is determined by the size of the aperture and the divergence of the undulator source, the so called geometrical shadow. Thus, the EXSU aperture is clipping the photon beam but has no effect on the focal beam size. In contrast, the Fresnel number for the BDA ranges from $N_F = 1.8$ to $N_F = 0.005$ at 780 eV photon energy for aperture sizes between 1 mm and 50 µm (53.1 m BDA to focus distance). In this Fresnel-number range a transition between Fresnel and Fraunhofer diffraction occurs. Below $N_F = 1$ (600 µm BDA), the shape of the photon beam changes and the divergence of the beam decreases, leading to a decreasing focal beam size. At small BDA sizes (≤ 150 µm) the divergence of the photon beam increases again due to Fraunhofer diffraction resulting in an increasing focal beam size. Hence, due to the impact of the BDA on the focal beam size it can be referred to as a secondary source.

The results of the systematic coherence analysis performed at the P04 beamline are shown in Fig. 6. For this analysis, a vertical EXSU aperture size of 30 µm has been used. For the variation of the BDA the horizontal EXSU aperture is set to fully open and vice versa. Upon closing the BDA to 50 µm, the coherent fraction ζ_x increases from $(13.6 \pm 1.5)\%$ to $(90.0 \pm 5.0)\%$ at 500 eV photon energy, from $(11.2 \pm 1.5)\%$ to $(95 \pm 3.5)\%$ at 780 eV photon energy, and from $(5.2 \pm 1.5)\%$ to $(53.0 \pm 4.0)\%$ at 1200 eV photon energy. Thus, for 500 eV and 780 eV photon energy the beam is almost fully coherent at an aperture size of 50 µm. At large BDA sizes (1 mm), the coherent fraction shows a very good agreement with the theoretical values of the undulator source (6.6%–12.9% (see Appendix A), dashed horizontal lines). The large increase of spatial coherence is directly correlated with an increase of the transverse coherence length $l_{s,x}$, which increases from (1.23 ± 0.04) µm to (20 ± 1.5) µm at 500 eV photon energy, from (0.89 ± 0.04) µm to (20 ± 1.5) µm at 780 eV photon energy, and from (0.45 ± 0.02) µm to (3.59 ± 0.25) µm at 1200 eV photon energy, at an aperture size of 50 µm. We find that the beam size decreases by decreasing the aperture from 1 mm to 50 µm. Thus, the increase of the coherent fraction is not only determined by an increasing transverse coherence length but also by an additional decrease of the beam size [see Eq. (5)]. For 500 eV, no decrease of the focal spot size is observed.

In contrast, at an aperture size of 200 μm, a small increase is observed. It is assumed that this behavior originates from the wavelength-dependent transition from Fresnel to Fraunhofer diffraction caused by the BDA. The Fresnel number is $N_F = 0.07$ for 500 eV, $N_F = 0.12$ for 780 eV, and $N_F = 0.2$ for 1200 eV at a BDA size of 200 μm. The transmission of the aperture drops significantly at BDA sizes < 200 μm. A high photon flux of around $5 \cdot 10^{10}$ ph/s is only maintained up to a coherent fraction ζ_x of around 46% at 500 eV, 33% at 780 eV, and 24% at 1200 eV, at a BDA size of 200 μm. Consequently, a higher coherent fraction is accompanied by a drop of orders of magnitude in photon flux [see Fig. 6].

For the other case, varying the EXSU beam-defining aperture and leaving the BDA open, we found an increase of the coherent fraction ζ_x from (8.2 ± 1.5)% to (59.3 ± 2.5)% at 500 eV photon energy and from (4.3 ± 1.5)% to (45.9 ± 2.5)% at 1200 eV photon energy with decreasing EXSU aperture size from fully open to 300 μm. This goes in line with an increase of the transverse coherence length $l_{s,x}$ from (0.91 ± 0.08) μm to (9.94 ± 0.19) μm at 500 eV, and from (0.45 ± 0.03) μm to (4.79 ± 0.13) μm at 1200 eV. In contrast to closing the BDA, the focal spot size remains unchanged when decreasing the EXSU size. This has been verified by using an additional beam diagnostic tool that is specifically designed to map out the full beam caustic of the X-ray beam with high spatial resolution, using a very thin Ce:YAG-screen coupled to a high resolution optics. This tool, however, can only be used interchangeably with the actual experimental setup. The small deviation of the focal spot size for 500 eV at an EXSU size of 3 mm results from a slight deformation of the beam profile. We find that the high coherent fraction of 60% at 500 eV and 46% at 1200 eV can be obtained while maintaining a photon flux higher than the one measured when using the BDA to obtain comparable spatial coherence. Assuming that the degree of spatial coherence of the source and of the photon beam along the propagation direction is constant, as proposed by the GSM, the relation between transmitted intensity and spatial degree of coherence should show the same trend for the BDA and EXSU aperture. However, the locations of both apertures at the beamline have a different effect on the photon-beam properties [53]. While the EXSU aperture is only clipping and selecting a coherent portion of the beam, the BDA additionally defines a secondary source and therewith controls the focal size. We assume that either the latter effect of the BDA requires a tighter clipping of the beam compared to the EXSU in order to increase the spatial degree of coherence, or the propagation of the highly spatially coherent beam at small BDA sizes along the whole beamline results in stronger interference effects at downstream optical elements (SMU, VLS, VKB, HKB), having an impact on the photon-beam profile and consequently on the measured photon flux.

So far, the vertical coherent fraction has not been addressed. The data shows that the vertical coherent fraction is between 41% and 54% and thus much smaller than expected (87%–91%) in the whole photon-energy range from 500 eV to 1200 eV (see Appendix A). Hence, notable spatial coherence degradation is observed in the vertical direction compared to the theoretical expectations. Possible sources of coherence degradation at the P04 beamline are discussed and analyzed in detail in the next section.

4.3. Sources of spatial-coherence degradation

Spatial-coherence degradation stands for a reduction of the (effective) spatial degree of coherence of the photon beam, originating from diverse sources within the beamline or the experiment [25,54,55]. One has to distinguish between direct and indirect coherence degradation. Direct coherence degradation denotes a reduction of the spatial coherence properties due to optical elements within the beamline, such that a lower spatial coherence is transported through the beamline and is available for experiments. This comprises, e.g., vibration-induced effects either in transmission (beryllium window, or graphite filter) [25,56,57] or reflection (monochromator, mirrors) [58–60], and the surface quality of optical elements [27,28]. Indirect coherence degradation implies the reduction of the observed coherence properties due to the experimental
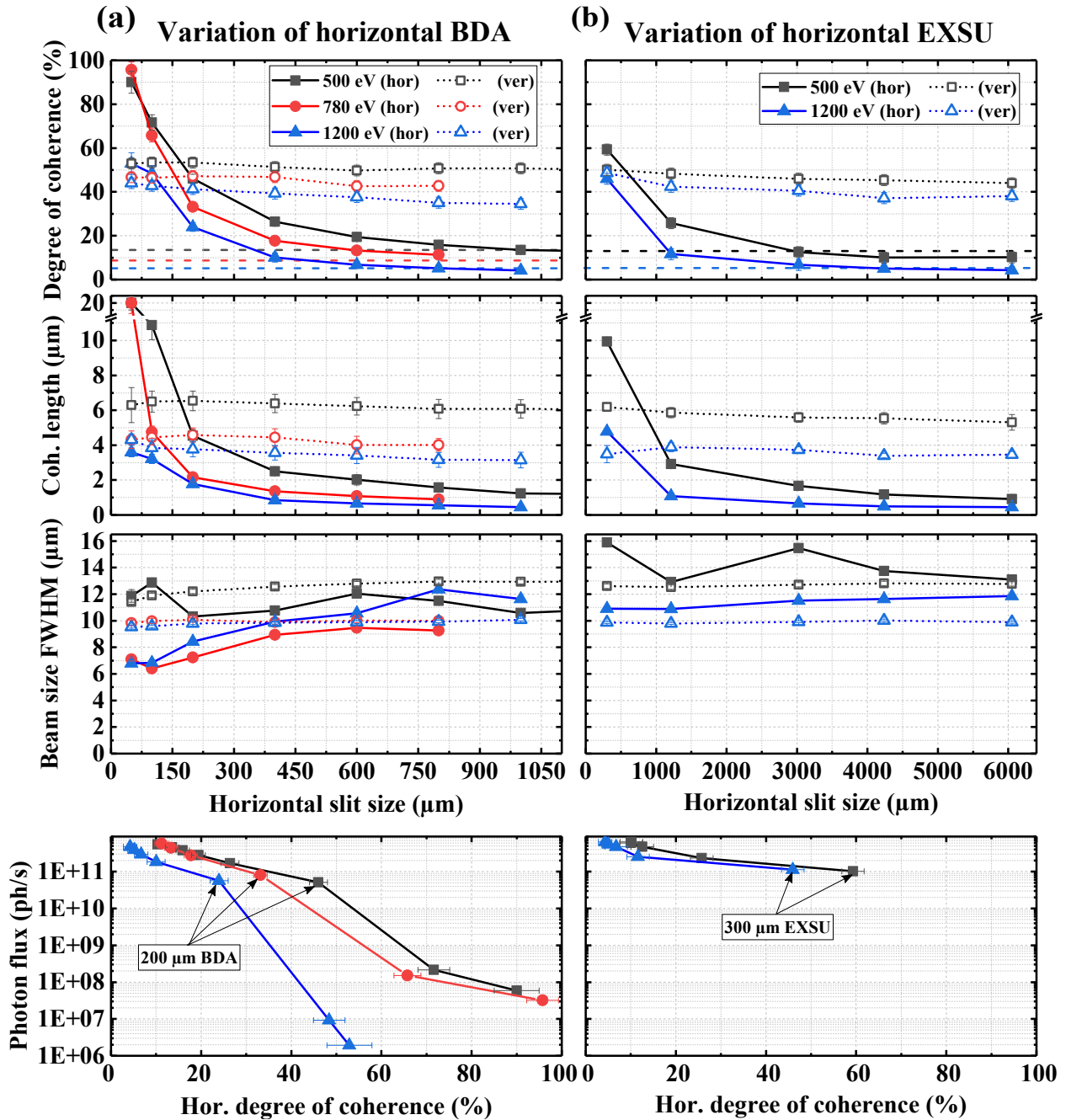
Fig. 6. (a) The degree of coherence, transverse coherence length, and focal beam size as a function of horizontal BDA openings as well as the photon flux as a function of the degree of coherence for three different photon energies [500 eV (black), 780 eV (red), and 1200 eV (blue)]. (b) The same dependencies presented in (a) but as a function of the horizontal EXSU aperture. In (a) and (b), the solid lines denote the horizontal, and the dotted lines the vertical axis. The dashed lines correspond to theoretical values for the degree of coherence of the undulator source (see Appendix A). For the variation of the BDA the EXSU aperture is set to fully open and vice versa.

apparatus and measurement technique, even though a higher spatial coherence is transported through the beamline. This includes vibrations of the sample or the sample stage, dynamics in the sample, insufficient longitudinal coherence, or under-sampling of speckles within the diffraction pattern.

For the performed Fourier-analysis experiment, indirect coherence degradation effects could be ruled out. The transverse coherence lengths determined from SAXS patterns recorded at different exposure times (0.05 s and 0.7 s, corresponding to 20 Hz and 1.4 Hz) does not show any deterioration [61]. A frequency analysis of photon beam vibrations at the focal position using the beam diagnostic tool mentioned in Section 4.2 shows vertical photon-beam vibrations with frequencies of 13 Hz, 18 Hz, 25 Hz, and 50 Hz, originating mainly from the VKB (The maximum resolvable frequency is 80 Hz). The distribution of the photon-beam movements reveals a Gaussian distribution with an rms width of 0.5 μm ($\stackrel{\wedge}{=}$ 100 nrad VKB pitch vibration). Frequencies faster than 20 Hz could not be analyzed in terms of spatial coherence in the experiment. However, using the model presented in Sections 3.1 and 3.2, we found that a movement of photon beam or sample by 0.5 μm (5% of the FWHM) has no effect on the position and size of the speckles within the modeled SAXS pattern. Hence, the results of the Fourier analysis are not affected by vibrations of that magnitude of the sample, the experimental chamber or the photon beam at the sample position.

However, vibrations of optical elements can have a profound impact on the spatial coherence properties, as these result in a significant increase of the virtual source size and hence directly influence the spatial coherence properties of the beam. Horizontal optical elements are less critical in terms of stability and due to the large undulator source size in the horizontal direction at most third-generation synchrotrons like PETRA III, vibrational effects on the horizontal spatial coherence properties are negligible. This is consistent with the fact that the horizontal spatial coherence for the full beam, determined by the analysis above, is in very good agreement with the theoretical values [see Fig. 6]. However, strong coherence degradation is observed in the vertical direction. At beamline P04, the only vertical optical elements are the VKB and the monochromator. The dispersive plane of the monochromator is in the vertical direction and hence vibrations of the monochromator cause small shifts of the photon energy, but no spatial vibrations of the beam in the focus. A check of the photon energy variations would require additional diagnostics [62]. The challenge is to precisely detect small energy variations at high frequencies to uncover the root cause of the vibrations.

The spatial-coherence degradation due to the vertical vibrations of the monochromator (pre-mirror and grating are considered separately), the VKB, and the undulator source can be calculated via the influence on the virtual source size by using Eq. (9) and following [31,53,63] to calculate the increased virtual source size $\Sigma_{\text{vib,y}}$ (rms) as

$$\Sigma_{\text{vib,y}} = \sqrt{\Sigma_y^2 + (2\sigma_{\text{PRE}}d_a)^2 + (2\sigma_{\text{GRT}}d_b)^2 + (3.68\sigma_{\text{VKB}}d_c)^2 + (\sigma_{SCR}^t)^2 + (\sigma_{SCR}^v)^2}. \quad (8)$$

Here, $d_a = 45.9$ m, $d_b = 46$ m, and $d_c = 7.5$ m are the source–pre-mirror, source–grating and EXSU–VKB distances, respectively. Further, σ_{PRE}, σ_{GRT}, σ_{VKB}, and σ_{SCR}^v are the rms values of the pitch vibrations of the pre-mirror, the grating, the VKB and the undulator source, respectively, while σ_{SCR}^t is the translational movement of the undulator source. The factor 2 for the pre-mirror pitch and grating pitch vibrations regards the twice as large deflection of the photon beam when pitching the mirror. The factor 3.68 for the VKB pitch vibrations reflects the optical demagnification of the monochromator in order to transform the VKB vibrations into virtual-source vibrations. The increased source divergence $\Sigma'_{\text{vib,y}}$ has been neglected as it has only a vanishingly small impact on the vertical coherent fraction. For the analytical calculation, upper limits for the optics vibrations have to be specified. An upper limit for the VKB vibration of $\sigma_{\text{VKB}} = 100$ nrad is found from the analysis above. The grating pitch vibration is limited to about $\sigma_{\text{GRT}} = 100$ nrad, which was determined using an autocollimator [39]. An upper limit for the

pre-mirror pitch vibrations σ_{PRE} can be estimated from the best energy resolution measured at a fixed vertical exit-slit size [62], which is ~ 40 meV at 1000 eV photon energy and 10 µm vertical exit-slit size. Using the ray-tracing software XRT (XRayTracer) [30], we find an upper limit of about σ_{PRE} ~ 200 nrad for the pre-mirror pitch vibrations. The source angular vibrations are of about $\sigma_{SCR}^{\mathrm{v}} = 50$ nrad and the source translational movements of around $\sigma_{SCR}^{\mathrm{v}} = 0.5$ µm (PETRA III archive viewer). We find that the contribution of the VKB vibration to $\Sigma_{\mathrm{vib,y}}$ is between 0.6%–1.4% and the contribution of the source angular vibration and translational movement to $\Sigma_{\mathrm{vib,y}}$ is below 0.1%. Thus, these contributions have only a vanishingly small effect on the calculated vertical coherent fraction. Figure 7 shows the calculated vertical coherent fraction as a function of the pre-mirror pitch vibrations σ_{PRE} for grating pitch vibrations of 100 nrad (solid line), 150 nrad (dashed line), and 200 nrad (dash-dotted line) at 500 eV (black), 780 eV (red), and 1200 eV (blue) photon energies. The dotted colored line represents the vertical coherent fraction ζ_{y} without vibrations of the optics or the undulator source, which are 90% at 500 eV, 89% at 780 eV, and 87% at 1200 eV photon energy. The calculated coherent fraction is significantly reduced from the values without vibrations to about 10%–20% at a pre-mirror pitch vibration of 1200 nrad. Using the determined upper limits of the optics vibrations, we find a reduction of the vertical coherent fraction ζ_{y} to about 70% at 500 eV, 62% at 780 eV, and 54% at 1200 eV photon energy. The vertical coherent fractions determined using the systematic spatial-coherence analysis show a very good agreement with the calculated vibrations of around 340 nrad for the pre-mirror pitch and 100 nrad for the grating pitch. This would result in an energy resolution of 65 meV using a 10 µm vertical exit-slit size which is much larger than the measured ~ 40 meV. As a consequence, the large deviations of the vertical coherent fractions in comparison with the theoretical values cannot be described only by optics vibrations.
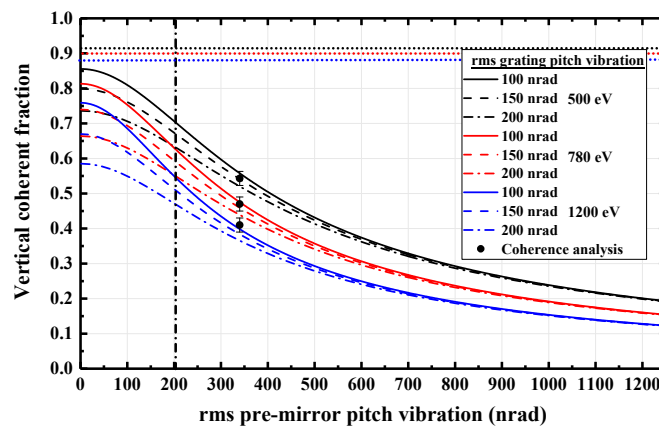
Fig. 7. Calculated vertical coherent fraction of the undulator source as a function of pre-mirror pitch vibrations (rms) for different grating pitch vibrations (rms) (100 nrad (solid lines), 150 nrad (dashed lines), and 200 nrad (dash-dotted lines) and three different photon energies [500 eV (black), 780 eV (red), and 1200 eV (blue)]. The black dots correspond to the measured vertical coherent fractions. The dotted lines represent the theoretical values of the undulator source (see Appendix A). The vertical dashed line corresponds to the independently determined upper limit of the pre-mirror pitch vibration.

Another source of spatial coherence degradation can be the quality of each optical element along the beamline. The photon beam from the undulator source can be re-scattered due to surface inhomogeneites of the optics or grating imperfections and can introduce unpredictable phase variations in the reflected beam. In [27,28], the authors propose that the imperfections of each optical element can be seen as a separate secondary source adding a further and almost

incoherent component superimposed on the original beam. The properties of the additional incoherent component depend strongly on the statistical parameters of the optics surface, e.g., surface roughness, and correlation length of the height–height fluctuations. Unfortunately, the magnitude of the effect is difficult to predict. The theory presented in [27] states that if the beam has a low degree of spatial coherence and can thus be seen as almost incoherent, the surface inhomogeneites have no effect on the coherence properties of the reflected beam, as the phase distribution of the incoming beam is already random. This can give a hint to the findings of Section 4.2, where the BDA has to be further closed compared to the EXSU aperture in order to improve the horizontal spatial-coherence properties of the photon beam. In case of the EXSU aperture, the beam is propagated through the beamline with a low spatial coherence until the far end of the beamline and hence upstream optical elements and their surface inhomogeneites have no effect on the spatial coherence properties of the beam. When closing the BDA, the spatial coherence properties are improved directly after the undulator and hence, depending on the degree of spatial coherence, each optical element of the beamline adds an incoherent component to the original beam leading to an effective spatial coherence degradation at the sample position.

5. Conclusions

We have presented a systematic multi-parameter 2D spatial-coherence analysis at the P04 beamline at PETRA III using the Fourier-analysis method. A spatially disordered nanodot array has been used as sample in order to overcome the wavelength restriction of the previous study [36]. For the systematic spatial-coherence analysis, three different photon energies (500 eV, 780 eV, and 1200 eV) have been used. Two different horizontal beamline apertures (BDA, EXSU) are utilized to vary the spatial coherence of the photon beam. We find that the spatial coherence can be increased up to 90% in the horizontal direction via closing the BDA down to 50 μm and up to 60% via closing the EXSU aperture down to 300 μm. It is observed that the increase of the coherent fraction using the BDA is accompanied by a decreasing focal beam size in the horizontal direction, down to a certain value and a decreasing photon flux. However, for the horizontal EXSU aperture, the beam size in the focus remains unchanged when varying its width, maintaining a still high photon flux. A strong spatial-coherence degradation to about 41%–54% is observed in the vertical direction. We find that a significant amount of this degradation can be ascribed to vibrations of the monochromator. However, the optics vibrations alone cannot fully explain the strong spatial coherence degradation. We assume that the surface quality of the optics and the re-scattering of the incoming beam have an additional significant contribution to the observed spatial coherence degradation. This effect will have to be further investigated in detail as it will have an increasing impact on future beamlines at DLSR facilities.

Appendix A

To give an exact description for the spatial coherence properties of synchrotron radiation from an undulator is a challenging task and heavily debated in the synchrotron community [47,64–69]. This is due to the fact that the emission of synchrotron radiation from an electron bunch in an undulator is described by statistically distributed wavefronts and is thus only partially coherent in most third-generation synchrotron facilities. The wavelength-dependent coherent fraction or global degree of coherence $\zeta(\lambda)$ of synchrotron radiation from an undulator is frequently described as the ratio of the diffraction-limited radiation emittance from a single electron $\varepsilon_r(\lambda)$ and the transverse radiation emittance of an ensemble of electrons or an electron bunch $\varepsilon_{x,y}(\lambda)$ [67]

$$\zeta(\lambda) = \frac{\varepsilon_r(\lambda)^2}{\varepsilon_x(\lambda)\varepsilon_y(\lambda)} = = \frac{\lambda^2}{4\pi^2 \Sigma_x \Sigma_x' \Sigma_y \Sigma_y'}. \tag{9}$$

$\Sigma_{x,y}$ and $\Sigma'_{x,y}$ are the photon-beam's source size and divergence which can be both calculated using the electron-beam emittance $\varepsilon_{x,y}(e^-)$, the betatron function $\beta_{x,y}$, and the magnetic length of the undulator L [67,70,71]. In literature different expressions exist for the spatial σ_r and angular $\sigma_{r'}$ representations of undulator radiation from a single electron; a comparison of all expressions can be found in [64]. Here, the expressions given by Onuki and Elleaume are used which result in the best agreement of analytically and numerically calculated coherent fractions [64,70]:

$$\sigma_r = \sqrt{\frac{\lambda L}{2\pi^2}}, \ \sigma_{r'} = \sqrt{\frac{\lambda}{2L}} \ \Rightarrow \ \varepsilon_r(\lambda) = \frac{\lambda}{2\pi}. \tag{10}$$

The coherent fraction of the synchrotron radiation emitted by the P04 APPLE-II undulator can be calculated using the parameters listed in Table 1 and Eq. (9). Figure 8 shows the calculated photon source size $\Sigma_{x,y}$ and divergence $\Sigma'_{x,y}$ (a) as well as the coherent fraction (b) as a function of photon energy. The coherent fraction is about 90% in the vertical direction and between 4% and 20% in the horizontal direction for the photon energy range covered by the beamline.
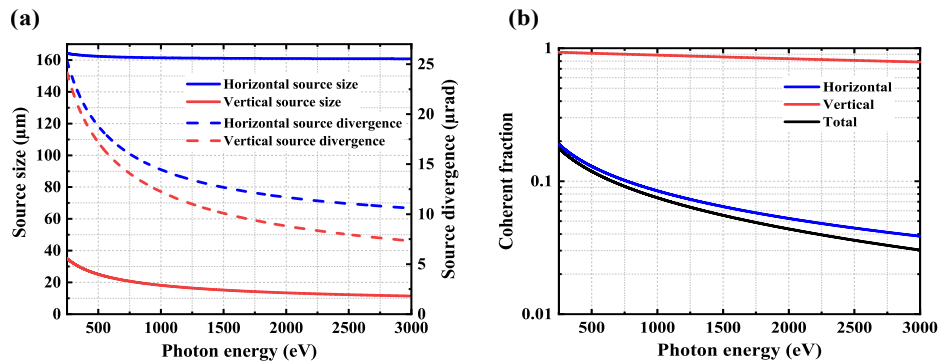
Fig. 8. (a) Calculated photon source size $\Sigma_{x,y}$ (solid lines) and source divergence $\Sigma'_{x,y}$ (dashed lines) of the P04 undulator at PETRA III as a function of photon energy. (b) Calculated horizontal (blue), vertical (red), and total (black) coherent fraction as a function of photon energy.

Table 1. PETRA III and P04 parameters.

Parameter	Horizontal (x)	Vertical (y)
Electron beam emittance $\varepsilon(e^-)$	1.29 nmrad	0.0129 nmrad
Betatron function β (High beta)	20.01 m	2.36 m
Undulator length L (P04)	4.75 m (magnets)	

Disclosures

The authors declare that there are no conflicts of interest related to this article.

References

1. C. G. Schroer, I. Agapov, W. Brefeld, R. Brinkmann, Y.-C. Chae, H.-C. Chao, M. Eriksson, J. Keil, X. Nuel Gavalda, R. Röhlsberger, O. H. Seeck, M. Sprung, M. Tischer, R. Wanzenberg, and E. Weckert, "PETRA IV: the ultralow-emittance source project at DESY," J. Synchrotron Radiat. **25**(5), 1277–1290 (2018).
2. C. Steier, "Possibilities for a diffraction-limited upgrade of a soft X-ray light source," Synchrotron Radiat. News **27**(6), 18–22 (2014).
3. C. Steier, A. Anders, D. Arbelaez, K. Baptiste, W. Barry, J. Byrd, K. Chow, S. de Santis, R. Duarte, R. Falcone, J.-Y. Jung, S. Kevan, S. Kwiatkowski, T. Luo, A. Madur, H. Nishimura, J. Osborn, C. Pappas, L. Reginato, D. Robin, F. Sannibale, R. Schlueter, C. Sun, C. Swenson, H. Tarawneh, W. Waldron, and W. Wan, "Proposal for a soft X-ray diffraction limited upgrade of the ALS," in Proceedings of IPAC2014 (JACoW, 2014), paper MOPME084.
4. P. Raimondi, "ESRF-EBS: The extremely brilliant source project," Synchrotron Radiat. News **29**(6), 8–15 (2016).
5. P. F. Tavares, S. C. Leemann, M. Sjöström, and A. Andersson, "The MAX IV storage ring project," J. Synchrotron Radiat. **21**(5), 862–877 (2014).
6. S. Eisebitt, J. Lüning, W. F. Schlotter, M. Lörgen, O. Hellwig, W. Eberhardt, and J. Stöhr, "Lensless imaging of magnetic nanostructures by X-ray spectro-holography," Nature **432**(7019), 885–888 (2004).
7. W. F. Schlotter, R. Rick, K. Chen, A. Scherz, J. Stöhr, J. Lüning, S. Eisebitt, C. Günther, W. Eberhardt, O. Hellwig, and I. McNulty, "Multiple reference Fourier transform holography with soft X rays," Appl. Phys. Lett. **89**(16), 163112 (2006).
8. D. Stickler, R. Frömter, H. Stillrich, C. Menk, C. Tieg, S. Streit-Nierobisch, M. Sprung, C. Gutt, L.-M. Stadler, O. Leupold, G. Grübel, and H. P. Oepen, "Soft X-ray holographic microscopy," Appl. Phys. Lett. **96**(4), 042501 (2010).
9. S. Streit-Nierobisch, D. Stickler, C. Gutt, L.-M. Stadler, H. Stillrich, C. Menk, R. Frömter, C. Tieg, O. Leupold, H. P. Oepen, and G. Grübel, "Magnetic soft X-ray holography study of focused ion beam-patterned Co/Pt multilayers," J. Appl. Phys. **106**(8), 083909 (2009).
10. A. P. Hitchcock, "Soft X-ray spectromicroscopy and ptychography," J. Electron Spectrosc. Relat. Phenom. **200**, 49–63 (2015).
11. X. Shi, P. Fischer, V. Neu, D. Elefant, J. C. T. Lee, D. A. Shapiro, M. Farmand, T. Tyliszczak, H.-W. Shiu, S. Marchesini, S. Roy, and S. D. Kevan, "Soft X-ray ptychography studies of nanoscale magnetic and structural correlations in thin SmCo5 films," Appl. Phys. Lett. **108**(9), 094103 (2016).
12. M. Rose, D. Dzhigaev, T. Senkbeil, A. R. von Gundlach, S. Stuhr, C. Rumancev, I. Besedin, P. Skopintsev, J. Viefhaus, A. Rosenhahn, and I. A. Vartanyants, "High-dynamic-range water window ptychography," J. Phys.: Conf. Ser. **849**, 012027 (2017).
13. J. M. Rodenburg, A. C. Hurst, A. G. Cullis, B. R. Dobson, F. Pfeiffer, O. Bunk, C. David, K. Jefimovs, and I. Johnson, "Hard-X-ray lensless imaging of extended objects," Phys. Rev. Lett. **98**(3), 034801 (2007).
14. Y. H. Lo, L. Zhao, M. Gallagher-Jones, A. Rana, J. J. Lodico, W. Xiao, B. C. Regan, and J. Miao, "In situ coherent diffractive imaging," Nat. Commun. **9**(1), 1826 (2018).
15. X. Tao, Z. Xu, H. Liu, C. Wang, Z. Xing, Y. Wang, and R. Tai, "Spatially correlated coherent diffractive imaging method," Appl. Opt. **57**(22), 6527–6533 (2018).
16. G. N. Tran, G. A. van Riessen, and A. G. Peele, "Modal approach for partially coherent diffractive imaging with simultaneous sample and coherence recovery," Opt. Express **25**(10), 10757–10764 (2017).
17. C. Jacobsen, S. Williams, E. Anderson, M. T. Browne, C. J. Buckley, D. Kern, J. Kirz, M. Rivers, and X. Zhang, "Diffraction-limited imaging in a scanning transmission x-ray microscope," Opt. Commun. **86**(3-4), 351–364 (1991).
18. M. D. de Jonge, B. Hornberger, C. Holzner, D. Legnini, D. Paterson, I. McNulty, C. Jacobsen, and S. Vogt, "Quantitative phase imaging with a scanning transmission X-ray microscope," Phys. Rev. Lett. **100**(16), 163902 (2008).
19. E. de Smit, I. Swart, J. F. Creemer, G. H. Hoveling, M. K. Gilles, T. Tyliszczak, P. J. Kooyman, H. W. Zandbergen, C. Morin, B. M. Weckhuysen, and F. M. F. de Groot, "Nanoscale chemical imaging of a working catalyst by scanning transmission X-ray microscopy," Nature **456**(7219), 222–225 (2008).
20. S. Chandran, N. Begam, M. Sprung, and J. K. Basu, "Coherent X-ray scattering reveals nature of dynamical transitions in nanoparticle–polymer suspensions," Polymer **105**, 500–509 (2016).
21. O. G. Shpyrko, "X-ray photon correlation spectroscopy," J. Synchrotron Radiat. **21**(5), 1057–1064 (2014).
22. D. L. Abernathy, G. Grübel, S. Brauer, I. McNulty, G. B. Stephenson, S. G. Mochrie, A. R. Sandy, N. Mulders, and M. Sutton, "Small-angle X-ray scattering using coherent undulator radiation at the ESRF," J. Synchrotron Radiat. **5**(1), 37–47 (1998).
23. X. Meng, X. Shi, Y. Wang, R. Reininger, L. Assoufid, and R. Tai, "Mutual optical intensity propagation through non-ideal mirrors," J. Synchrotron Radiat. **24**(5), 954–962 (2017).
24. K. A. Nugent, C. Q. Tran, and A. Roberts, "Coherence transport through imperfect X-ray optical systems," Opt. Express **11**(19), 2323–2328 (2003).
25. M. Yabashi, K. Tono, H. Mimura, S. Matsuyama, K. Yamauchi, T. Tanaka, H. Tanaka, K. Tamasaku, H. Ohashi, S. Goto, and T. Ishikawa, "Optics for coherent X-ray applications," J. Synchrotron Radiat. **21**(5), 976–985 (2014).

26. U. H. Wagner, A. Parson, and C. Rau, "Coherence length and vibrations of the coherence beamline I13 at the diamond light source," J. Phys.: Conf. Ser. **849**, 012048 (2017).

27. I. A. Vartanyants and I. K. Robinson, "Origins of decoherence in coherent X-ray diffraction experiments," Opt. Commun. **222**(1-6), 29–50 (2003).

28. I. K. Robinson, C. A. Kenney-Benson, and I. A. Vartanyants, "Sources of decoherence in beamline optics," Phys. B (Amsterdam, Neth.) **336**(1-2), 56–62 (2003).

29. O. Chubar, A. Fluerasu, L. Berman, K. Kaznatcheev, and L. Wiegart, "Wavefront propagation simulations for beamlines and experiments with "Synchrotron Radiation Workshop"," J. Phys.: Conf. Ser. **425**(16), 162001 (2013).

30. K. Klementiev and R. Chernikov, "Powerful scriptable ray tracing package xrt," Proc. SPIE **9209**, 92090A (2014).

31. X. Shi, R. Reininger, M. S. del Rio, and L. Assoufid, "A hybrid method for X-ray optics simulation: combining geometric ray-tracing and wavefront propagation," J. Synchrotron Radiat. **21**(4), 669–678 (2014).

32. E. J. Jaeschke, S. Khan, J. R. Schneider, and J. B. Hastings, eds., *Synchrotron light sources and free-electron lasers. Accelerator physics, instrumentation and science applications*, Part IV (Springer, 2016).

33. M. D. Alaimo, M. A. C. Potenza, M. Manfredda, G. Geloni, M. Sztucki, T. Narayanan, and M. Giglio, "Probing the transverse coherence of an undulator X-ray beam using Brownian particles," Phys. Rev. Lett. **103**(19), 194805 (2009).

34. Y. Kashyap, H. Wang, and K. Sawhney, "Two-dimensional transverse coherence measurement of hard-X-ray beams using near-field speckle," Phys. Rev. A **92**(3), 033842 (2015).

35. S. Xianbo, M. Shashidhara, J. W. Michael, G. K. Naresh, T. M. Albert, and A. Lahsen, "Circular grating interferometer for mapping transverse coherence area of X-ray beams," Appl. Phys. Lett. **105**(4), 041116 (2014).

36. K. Bagschik, R. Frömter, L. Müller, W. Roseker, J. Bach, P. Staeck, C. Thönnißen, S. Schleitzer, M. H. Berntsen, C. Weier, R. Adam, J. Viefhaus, C. M. Schneider, G. Grübel, and H. P. Oepen, "Spatial coherence determination from the Fourier analysis of a resonant soft X-ray magnetic speckle pattern," Opt. Express **24**(20), 23162–23176 (2016).

37. A. Singer, U. Lorenz, A. Marras, A. Klyuev, J. Becker, K. Schlage, P. Skopintsev, O. Gorobtsov, A. Shabalin, H.-C. Wille, H. Franz, H. Graafsma, and I. A. Vartanyants, "Intensity interferometry of single X-ray pulses from a synchrotron storage ring," Phys. Rev. Lett. **113**(6), 064801 (2014).

38. A. Singer, U. Lorenz, F. Sorgenfrei, N. Gerasimova, J. Gulden, O. M. Yefanov, R. P. Kurta, A. Shabalin, R. Dronyak, R. Treusch, V. Kocharyan, E. Weckert, W. Wurth, and I. A. Vartanyants, "Hanbury Brown-Twiss interferometry at a free-electron laser," Phys. Rev. Lett. **111**(3), 034802 (2013).

39. J. Viefhaus, F. Scholz, S. Deinert, L. Glaser, M. Ilchen, J. Seltmann, P. Walter, and F. Siewert, "The Variable Polarization XUV Beamline P04 at PETRA III: Optics, mechanics and their performance," Nucl. Instrum. Methods Phys. Res., Sect. A **710**, 151–154 (2013).

40. K. Bagschik, R. Frömter, J. Bach, B. Beyersdorff, L. Müller, S. Schleitzer, M. H. Berntsen, C. Weier, R. Adam, J. Viefhaus, C. M. Schneider, G. Grübel, and H. P. Oepen, "Employing soft X-ray resonant magnetic scattering to study domain sizes and anisotropy in Co/Pd multilayers," Phys. Rev. B **94**(13), 134413 (2016).

41. A. Neumann, N. Franz, G. Hoffmann, A. Meyer, and H. P. Oepen, "Fabrication of magnetic Co/Pt nanodos utilizing filled diblock copolymers," Open Surf. Sci. J. **4**(1), 55–64 (2012).

42. H. Stillrich, A. Frömsdorf, S. Pütter, S. Förster, and H. P. Oepen, "Sub-20 nm magnetic dots with perpendicular magnetic anisotropy," Adv. Funct. Mater. **18**(1), 76–81 (2008).

43. J. Als-Nielsen and D. McMorrow, *Elements of modern X-ray physics*, 2nd ed. (Wiley, 2011).

44. I. A. Vartanyants and I. K. Robinson, "Imaging of quantum array structures with coherent and partially coherent diffraction," J. Synchrotron Radiat. **10**(6), 409–415 (2003).

45. T. Latychevskaia, G. F. Mancini, and F. Carbone, "The role of the coherence in the cross-correlation analysis of diffraction patterns from two-dimensional dense mono-disperse systems," Sci. Rep. **5**(1), 16573 (2015).

46. L. Mandel and E. Wolf, *Optical coherence and quantum optics* (Cambridge University, 1995).

47. I. A. Vartanyants and A. Singer, "Coherence properties of hard X-ray synchrotron sources and X-ray free-electron lasers," New J. Phys. **12**(3), 035004 (2010).

48. P. Skopintsev, A. Singer, J. Bach, L. Müller, B. Beyersdorff, S. Schleitzer, O. Gorobtsov, A. Shabalin, R. P. Kurta, D. Dzhigaev, O. M. Yefanov, L. Glaser, A. Sakdinawat, G. Grübel, R. Frömter, H. P. Oepen, J. Viefhaus, and I. A. Vartanyants, "Characterization of spatial coherence of synchrotron radiation with non-redundant arrays of apertures," J. Synchrotron Radiat. **21**(4), 722–728 (2014).

49. G. J. Williams, O. Chubar, I. K. Robinson, L. Berman, and Y. S. Chu, "Optical design and simulation of a new coherence beamline at NSLS-II," Proc. SPIE **10388**, 103880E (2017).

50. O. Chubar, M. S. Rakitin, Y.-C. Chen-Wiegart, A. Fluerasu, and L. Wiegart, "Simulation of experiments with partially coherent X-rays using synchrotron radiation workshop," Proc. SPIE **10388**, 1038811 (2017).

51. S. Roling, B. Siemer, M. Wöstmann, H. Zacharias, R. Mitzner, A. Singer, K. Tiedtke, and I. A. Vartanyants, "Temporal and spatial coherence properties of free-electron-laser pulses in the extreme ultraviolet regime," Phys. Rev. Spec. Top.–Accel. Beams **14**(8), 080701 (2011).

52. M. Born, E. Wolf, A. B. Bhatia, P. C. Clemmow, D. Gabor, A. R. Stokes, A. M. Taylor, P. A. Wayman, and W. L. Wilcock, *Principles of optics* (Cambridge University, 1999).

53. X. Shi, R. Reininger, R. Harder, and D. Haeffner, "X-ray optics simulation and beamline design for the APS upgrade," Proc. SPIE **10388**, 103880C (2017).

54. V. Kohn, I. Snigireva, and A. Snigirev, "Direct measurement of transverse coherence length of hard X rays from interference fringes," Phys. Rev. Lett. **85**(13), 2745–2748 (2000).

55. Y. Wang, T. Xiao, and H. Xu, "Effect of surface roughness on the spatial coherence of X-ray beams from third-generation synchrotron radiation sources," J. Synchrotron Radiat. **7**(4), 209–214 (2000).

56. A. Snigirev, I. Snigireva, V. G. Kohn, and S. M. Kuznetsov, "On the requirements to the instrumentation for the new generation of the synchrotron radiation sources. Beryllium windows," Nucl. Instrum. Methods Phys. Res., Sect. A **370**(2-3), 634–640 (1996).

57. M. Yabashi, K. Tamasaku, and T. Ishikawa, "Characterization of the transverse coherence of hard synchrotron radiation by intensity interferometry," Phys. Rev. Lett. **87**(14), 140801 (2001).

58. H. Mimura, K. Yamauchi, K. Yamamura, A. Kubota, S. Matsuyama, Y. Sano, K. Ueno, K. Endo, Y. Nishino, K. Tamasaku, M. Yabashi, T. Ishikawa, and Y. Mori, "Image quality improvement in a hard X-ray projection microscope using total reflection mirror optics," J. Synchrotron Radiat. **11**(4), 343–346 (2004).

59. J. I. Espeso, P. Cloetens, J. Baruchel, J. Härtwig, T. Mairs, J. C. Biasci, G. Marot, M. Salomé-Pateyron, and M. Schlenker, "Conserving the coherence and uniformity of third-generation synchrotron radiation beams: the case of ID19, a 'long' beamline at the ESRF," J. Synchrotron Radiat. **5**(5), 1243–1249 (1998).

60. Z. Guo, X. Meng, Y. Wang, H. Liu, X. Zhang, Z. Li, L. Xue, and R. Tai, "Effects of temperature, mechanical motion and source positional jitter on the resolving power of beamline 02B at the SSRF," J. Synchrotron Radiat. **24**(4), 877–885 (2017).

61. W. Grizolli, X. Shi, and L. Assoufid, "Influence of optics vibration on synchrotron beam coherence," Opt. Lett. **44**(4), 899–902 (2019).

62. J. Buck, K. Bagschik, L. Glaser, F. Scholz, J. Seltmann, and J. Viefhaus, "Progress report on the XUV online diagnostic unit for the highly accurate determination of SR properties," AIP Conf. Proc. **2054**, 060057 (2019).

63. S. Goto, "Effect of beamline optics vibration on the source size and divergence for synchrotron radiation," Proc. SPIE **9588**, 95880G (2015).

64. M. Sanchez del Rio, "About the coherent fraction of synchrotron emission," http://arxiv.org/pdf/1801.07542v2.

65. K.-J. Kim, "Characteristics of synchrotron radiation," AIP Conf. Proc. **184**, 565–632 (1989).

66. K.-J. Kim, "Angular distribution of undulator power for an arbitrary deflection parameter K," Nucl. Instrum. Methods Phys. Res., Sect. A **246**(1-3), 67–70 (1986).

67. R. Hettel, "Challenges in the design of diffraction-limited storage rings," in *Proceedings of IPAC2014* (JACoW, 2014), paper MOXBA01.

68. T. Tanaka and H. Kitamura, "Universal function for the brilliance of undulator radiation considering the energy spread effect," J. Synchrotron Radiat. **16**(3), 380–386 (2009).

69. K.-J. Kim, "Brightness, coherence and propagation characteristics of synchrotron radiation," Nucl. Instrum. Methods Phys. Res., Sect. A **246**(1-3), 71–76 (1986).

70. P. Elleaume and H. Onuki, *Undulators, wigglers and their applications* (Taylor and Francis, 2003).

71. M. Bei, M. Borland, Y. Cai, P. Elleaume, R. Gerig, K. Harkay, L. Emery, A. Hutton, R. Hettel, R. Nagaoka, D. Robin, and C. Steier, "The potential of an ultimate storage ring for future light sources," Nucl. Instrum. Methods Phys. Res., Sect. A **622**(3), 518–535 (2010).